Monthly Notices
of the
ROYAL ASTRONOMICAL SOCIETY

MNRAS **458,** 772–780 (2016) doi:10.1093/mnras/stw345

Spatially resolved dust emission of extremely metal-poor galaxies*

Luwenjia Zhou,[1,2]★ Yong Shi,[1,2,3]★ Taino Diaz-Santos,[4] Lee Armus,[5] George Helou,[5] Sabrina Stierwalt[6] and Aigen Li[7]

[1]*School of Astronomy and Space Science, Nanjing University, Nanjing 210093, China*
[2]*Key Laboratory of Modern Astronomy and Astrophysics (Nanjing University), Ministry of Education, Nanjing 210093, China*
[3]*Collaborative Innovation Center of Modern Astronomy and Space Exploration, Nanjing 210093, China*
[4]*Nu Ìcleo de Astronom a de la Facultad de Ingenier a, Universidad Diego Portales, Av. Ej Ìercito Libertador 441, Santiago, Chile*
[5]*Infrared Processing and Analysis Center, California Institute of Technology, 1200 E. California Boulevard, Pasadena, CA 91125, USA*
[6]*Department of Astronomy, University of Virginia, PO Box 400325, Charlottesville, VA 22904, USA*
[7]*Department of Physics and Astronomy, University of Missouri, Columbia, MO 65211, USA*

Accepted 2016 February 10. Received 2016 February 10; in original form 2015 November 19

ABSTRACT

We present infrared (IR) spectral energy distributions (SEDs) of individual star-forming regions in four extremely metal-poor (EMP) galaxies with metallicity $Z \lesssim Z_{\odot}/10$ as observed by the *Herschel Space Observatory*. With the good wavelength coverage of the SED, it is found that these EMP star-forming regions show distinct SED shapes as compared to those of grand design Spirals and higher metallicity dwarfs: they have on average much higher $f_{70\,\mu m}/f_{160\,\mu m}$ ratios at a given $f_{160\,\mu m}/f_{250\,\mu m}$ ratio; single modified blackbody (MBB) fittings to the SED at $\lambda \geq 100\ \mu$m still reveal higher dust temperatures and lower emissivity indices compared to that of Spirals, while two MBB fittings to the full SED with a fixed emissivity index ($\beta = 2$) show that even at 100 μm, about half of the emission comes from warm (50 K) dust, in contrast to the cold (∼20 K) dust component. Our spatially resolved images furthermore reveal that the far-IR colours including $f_{70\,\mu m}/f_{160\,\mu m}$, $f_{160\,\mu m}/f_{250\,\mu m}$ and $f_{250\,\mu m}/f_{350\,\mu m}$ are all related to the surface densities of young stars as traced by far-UV, 24 μm and star formation rates (SFRs), but not to the stellar mass surface densities. This suggests that the dust emitting at wavelengths from 70 to 350 μm is primarily heated by radiation from young stars.

Key words: galaxies: dwarf – galaxies: ISM.

1 INTRODUCTION

Stars born within primordial galaxies in the early Universe form out of gas with no or little metals. These distant galaxies are, however, difficult to detect. Nearby extremely metal-poor (EMP) star-forming galaxies are chemically unevolved, and thus offer important astrophysical laboratories for our understandings of the interstellar medium (ISM) and star formation in the low-metallicity environments (Kunth & Oumlstlin 2000; Rémy-Ruyer et al. 2013; Shi et al. 2014, 2015). Dust grains play a vital role in galaxy formation and evolution. Characterizing the dust properties by investigating the infrared (IR) emission is a powerful way to understanding the ISM and evolution of dwarf galaxies (Feldmann 2015).

The integrated dust properties of dwarfs have been investigated with *Spitzer Space Telescope*. It is found that aromatic features are absent in the metal-poor galaxies. Engelbracht et al. (2005) pointed out that the ratio $f_{8\,\mu m}/f_{24\,\mu m}$ depends strongly on the metallicity (where f_{λ} is the flux density at wavelength λ), with significantly lower values (mean ratio 0.08 ± 0.04) for galaxies below one-third of the Solar metallicity than those at higher metallicities (mean ratio 0.70 ± 0.53).[1] Draine & Li (2007) confirmed no polycyclic aromatic hydrocarbons emission in low-metallicity galaxies, as well as other works (e.g. Wu et al. 2006; Rosenberg et al. 2008). The H I-to-dust mass ratio as studied by Engelbracht et al. (2008) is shown to increase with the decreasing metallicity to 12+log(O/H)∼8, as $\sim Z^{-2.5}$, and flattens out at lower oxygen abundances. They also found an anti-correlation between dust temperature[2] and metallicity up to 12+log(O/H) ∼ 8, from $T \sim 23$ K near the Solar metallicity to $T \sim 40$ K at lower metallicity, but a positive relation at lower metallicities.

* *Herschel* is an ESA space observatory with science instruments provided by European-led Principal Investigator consortia and with important participation from NASA.

★E-mail: zhoulwj@gmail.com (LZ); yong@nju.edu.cn (YS)

[1] Engelbracht et al. (2005) adopted Solar metallicity as $12 + \log(O/H) = 8.7$ (Allende Prieto, Lambert & Asplund 2001). Here in this paper, we define Solar metallicity to be 8.7 as well. Thus, one-third of the Solar metallicity is around 8.2.

[2] Temperatures are derived from modified blackbody (MBB), with the emissivity index β fixed to be 2.

Table 1. Properties of our four EMP galaxies along with additional two galaxies from the literature.

Name	Distance (Mpc)	Metallicity 12+log(O/H)	Morphology
SextansA	1.4	7.49	dIrr
ESO146−G14	21.4	7.61	LSB
DDO 68	5.9	7.21	BCD
Ho II	3.3	7.92	dIrr
I Zw 18	18.2[a]	7.14[b]	BCD
SBS 0335-052	56.0[c]	7.25[d]	BCD

Notes. [a]Aloisi et al. (2007); [b]Izotov & Thuan (1999); [c]Madden et al. (2013); [d]Izotov et al. (1997).

The *Herschel Space Observatory* furthermore extends the wavelength coverage into the far-IR and sub-millimeter wavelengths, which combined with the *Spitzer* photometry significantly improves the measurement of the dust properties. The total gas-to-dust ratio as revealed by *Herschel* increases the decreasing metallicity. The slope of the relationship is −1 at higher metallicity (12+log(O/H) > 8) and becomes even steeper at the lower metallicity end (Rémy-Ruyer et al. 2014). It is also found that the metal content may not be the only factor affecting the dust properties of dwarfs. For example, the dust to stellar mass ratio of IZw 18 and SBS 0335-052, which have similar metallicities to the other EMP galaxies in Table 1, are very different (10^{-6}–10^{-5}, and 10^{-3}–10^{-2}, respectively) as estimated by Fisher et al. (2014) and Hunt et al. (2014), respectively. The ratio for IZw 18 is extremely low, while that for SBS 0335-052 is comparable to that found for normal Spiral galaxies (Hunt et al. 2014).

While significant progresses have been made in understanding the integrated dust properties of EMP galaxies, spatially resolved investigations of dust properties of these galaxies are still rare, and thus, the dependence of dust properties on the local condition is largely unconstrained in the EMP galaxies. In this study, we aim to benefit from the high spatial resolution of the *Herschel Space Observatory* to investigate the IR emission of individual star-forming regions of four EMP galaxies, with focus on the IR spectral energy distribution (SED) shapes and their relations to the local conditions.

2 SAMPLE, OBSERVATIONS AND DATA ANALYSIS

2.1 The sample

Our sample of EMP galaxies contains four objects including Sextans A, ESO 146−G14, DDO 68 and Holmberg II (Ho II). Sextans A is a dwarf irregular at 1.4 Mpc with 12+log(O/H)=7.49 based on the direct method (Kniazev et al. 2005). ESO 146−G14 with a direct method based 12+log(O/H)=7.61 (Bergvall & Ronnback 1995) is a blue low-surface brightness galaxy at a distance of 21.4 Mpc. DDO 68 with a direct method based 12+log(O/H)=7.21 (Pustilnik, Kniazev & Pramskij 2005) is a blue compact dwarf at a distance of 5.9 Mpc. Ho II is a Magellanic irregular dwarf at a distance of 3.3 Mpc (McCall et al. 2012), with a direct method based 12+log(O/H)=7.92 (Croxall et al. 2009).

We also compared our results to the integrated measurements of the Key Insights on Nearby Galaxy: A Far-Infrared Survey with Herschel (KINGFISH) sample (Kennicutt et al. 2011), the DGS (Dwarf Galaxy Survey) sample (Madden et al. 2013), and other two EMP galaxies (I Zw 18 and SBS 0335-052). These properties are listed in Table 1.

Table 2. Exposure time of *Herschel* data used in this paper.

Name	PACS 70, 160 μm	SPIRE 250, 350, 500 μm
SextansA	1.9 h	6 min
ESO146−G14	1.6 h	6 min
DDO 68	2.7 h	10 min

2.2 Observations

Herschel broad-band images (PI: Y. Shi, PID: OT2_yshi_3) of Sextans A, ESO 146−G14 and DDO 68 were taken at 70 and 160 μm through the scan map modes of PACS (Poglitsch et al. 2010), and 250, 350 and 500 μm through the small map modes with Spectral and Photometric Imaging Receiver (SPIRE) (Griffin et al. 2010). The exposure time (excluding overheads) in the two Photodetector Array Camera and Spectrometer (PACS) bands is 1.9, 1.6 and 2.7 h for Sextans A, ESO 146−G14 and DDO 68, respectively, and in the three SPIRE bands is 6, 6 and 10 min, respectively. The data of Sextans A and ESO 146−G14 have been partly published in Shi et al. (2014) where the detailed data reduction was given, while the data of DDO 68 are newly presented here. DDO 68 has low S/N, which may cause large uncertainties on the colour (Section 3). The PACS and SPIRE integration times of the observations are also listed in in Table 2. The *Herschel* data of HoII were taken from the KINGFISH project (Kennicutt et al. 2011).

In addition to the *Herschel* data, the *Spitzer* IR data at 24 μm and *GALEX* far-UV (FUV) data at 1516 Å were also retrieved from the archive.

2.3 Photometric measurements

As detailed in Shi et al. (2014), the star-forming disc of each galaxy is defined as an ellipse/circle to closely follow the 10σ contour of the FUV emission, as shown in Fig. 1. Note that, for DDO 68, we excluded the tidal tail to better focus on the main disc, although the tail is formally above the 10σ detection threshold. Individual dusty star-forming clumps within a star-forming disc were identified as circle regions with elevated FUV and 160 μm IR emission which is 3σ above the fluctuations of the disc emission. The defined star-forming regions are listed in Table 3. For the flux measurements, the underlying sky emission is estimated within a sky annuli between 1.1 and 1.5 times the disc aperture. For flux error estimates, the *Herschel* flux uncertainty is given by the following sources: the first is the uncertainty of the photon noise within the aperture we defined; the second is the uncertainty from the sky background subtraction; the third represents the uncertainty introduced by the offset from the accurate point spread function (PSF) position when we defined the aperture for each source; and the system uncertainty is also included. For more details, please see Shi et al. (2014). The measurements of fluxes at other wavelengths basically follow the same procedure. The photometric results of these star-forming regions are listed in Table 3.

In order to compare images among different resolutions, aperture corrections are performed on all the star-forming clumps based on their PSFs. We have tested that the aperture correction method has almost the same effect as convolving images to the same resolution

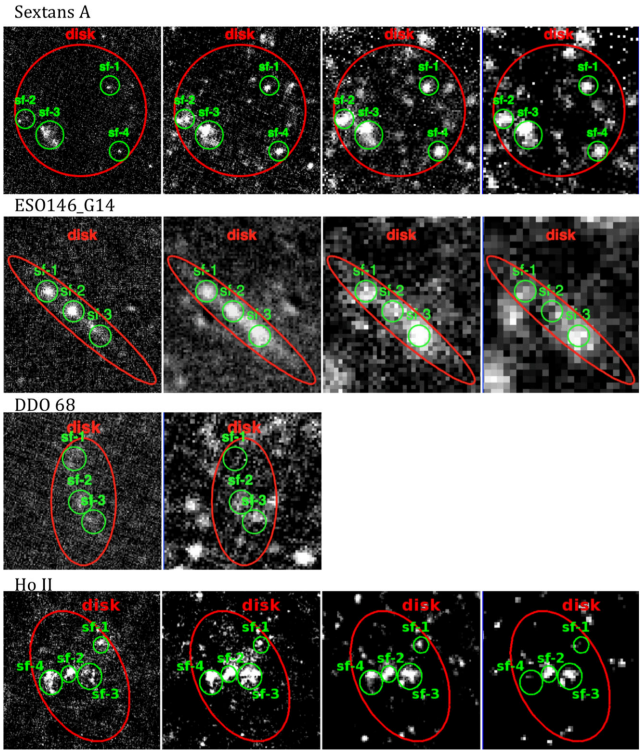

Figure 1. The *Herschel* images of our galaxies at 70, 160, 250 and 350 μm from left to right. The large ellipses indicate the extension of the whole star-forming disc and small circles are those individual dusty star-forming regions.

when fitting spectral energy distributions (SEDs; e.g. see Casasola et al. 2015). Pixel sizes and resolutions of images at each wavelength are listed in Table 4.

3 THE FAR-IR SEDs

3.1 The –colour diagrams

Fig. 2 shows the $f_{70\,\mu m}/f_{160\,\mu m}$ versus $f_{160\,\mu m}/f_{250\,\mu m}$ colour–colour diagram of our individual EMP regions along with those integrated measurements of the KINGFISH and DGS galaxies. The predictions of single MBB models are overlaid as grids, where the solid line represents a constant emissivity index, β, with the temperature ranging from 10 to 100 K in decrements of 5 K from the left-bottom to the upper-right, and the dashed lines represent constant temperatures with β ranging from 0.0 to 3.0 in steps of 0.5 from the left-bottom to the upper-right. The included DGS galaxies are those with $Z/Z_{\odot}$ above ∼10 per cent, because those EMP ones in their sample lack the enough S/N (≥3) to be included. As indicated by Fig. 2, our sample shows a quite different behaviour as compared to the DGS and KINGFISH Spirals. The majority of the KINGFISH locates in the region with $f_{70\,\mu m}/f_{160\,\mu m} < 1.5$ and $f_{160\,\mu m}/f_{250\,\mu m} < 2.5$, and the DGS ranges from the bottom-left to the upper-right, confined by the overlaid grey-body curves. In contrast, our EMP regions mainly occupy the left side of the plot, with $f_{160\,\mu m}/f_{250\,\mu m} < 2$ but $f_{70\,\mu m}/f_{160\,\mu m}$ covers a range from 0 to 2.5. At given $f_{160\,\mu m}/f_{250\,\mu m}$, our sample shows a much larger scatter in $f_{70\,\mu m}/f_{160\,\mu m}$, and more dramatically, a large fraction of our sample has $f_{70\,\mu m}/f_{160\,\mu m}$ above the limit of a single MBB with $\beta = 0$ (that is the blackbody emission) for a given $f_{160\,\mu m}/f_{250\,\mu m}$. When compared with the trend of star-forming galaxies predicted by empirical models of Dale et al. (2014), the median behaviour of KINGFISH and DGS basically follow the trend, while star-forming regions of our EMP galaxies lie systematically above the trend. A reasonable explanation for the large $f_{70\,\mu m}/f_{160\,\mu m}$ ratio is an excess of $f_{70\,\mu m}$ emission contributed by an additional source of heating. The stochastically heated small grains may be responsible for the excess 70 μm emission (Draine & Li 2001). The requirement of a second heating component when performing a fit to the 70–500 μm photometry has been widely seen in all types of galaxies (Galametz et al. 2012; Rémy-Ruyer et al. 2013), while our sample seems to be the extreme case in which about half of our sample has $f_{70\,\mu m}/f_{160\,\mu m}$ higher than the blackbody curve for a given $f_{160\,\mu m}/f_{250\,\mu m}$ colour.

Similar to Fig. 2, Fig. 3 presents another colour–colour plot that is $f_{160\,\mu m}/f_{250\,\mu m}$ versus $f_{250\,\mu m}/f_{350\,\mu m}$. Again, our EMP regions occupy a different area of the diagram, when compared with the other two sample. The KINGFISH Spirals and DGS galaxies span a similar range of $f_{250\,\mu m}/f_{350\,\mu m}$ but the latter shows larger $f_{160\,\mu m}/f_{250\,\mu m}$ at given $f_{250\,\mu m}/f_{350\,\mu m}$ compared to the former. In contrast, our EMP regions mainly occupy the locus towards the

Table 3. Photometry of individual star-forming regions in metal poor galaxies.

Region[a]	Position (J2000)[b]	$m_a \times m_b$[c] (arcsec^2)	f_{FUV}[d] (μJy)	$f_{3.6\,\mu m}$ (mJy)	$f_{4.5\,\mu m}$ (mJy)	$f_{24\,\mu m}$ (mJy)	$f_{70\,\mu m}$ (mJy)	$f_{100\,\mu m}$ (mJy)	$f_{160\,\mu m}$ (mJy)	$f_{250\,\mu m}$ (mJy)	$f_{350\,\mu m}$
SextansA/sf-1	10:10:56.9 − 04:40:27.0	22×22	960 ± 0.4	1.64 ± 0.009	1.05 ± 0.008	1.06 ± 0.14	41 ± 2		56±7	55±3	32±3
Se×tansA/sf-2	10:11:10.0 − 04:41:44.5	22×22	660 ± 0.4	1.65 ± 0.009	1.36 ± 0.008	3.22 ± 0.33	72 ± 3		147±18	111±4	52±4
Se×tansA/sf-3	10:11:6.20 − 04:42:22.5	32×32	4300 ± 0.6	2.78 ± 0.013	2.20 ± 0.011	6.30 ± 0.64	267 ± 4		297±24	164±5	89±4
Se×tansA/sf-4	10:10:55.5 − 04:42:59.4	22×22	260 ± 0.4	1.14 ± 0.009	0.69 ± 0.008	0.94 ± 0.13	21 ± 2		69±8	62±3	34±3
ESO146−G14/sf-1	22:13:6.0 − 62:03:32.5	10×10	150 ± 0.2	0.33 ± 0.003	0.24 ± 0.003	1.02 ± 0.16	28 ± 4		38±6	29±4	16±3
ESO146−G14/sf-2	22:13:2.5 − 62:03:51.6	10×10	260 ± 0.2	0.38 ± 0.003	0.28 ± 0.003	1.23 ± 0.18	36 ± 5		52±8	28±3	11±3
ESO146−G14/sf-3	22:12:59.0 − 62:04:14.3	10×10	90 ± 0.2	0.74 ± 0.003	0.50 ± 0.003	0.91 ± 0.16	15 ± 2		57±9	49±6	31±4
DDO68/sf-a	09:56:46.6 + 28:50:16.6	10×10	340 ± 0.1	0.08 ± 0.004	0.08 ± 0.006	0.71 ± 0.08	11 ± 1		<2	<5	<5
DDO68/sf-b	09:56:46.2 + 28:49:39.6	10×10	370 ± 0.1	0.41 ± 0.004	0.25 ± 0.006	0.36 ± 0.05	10 ± 1		9±1	<5	<5
DDO68/sf-c	09:56:45.3 + 28:49:22.6	10×10	350 ± 0.1	0.60 ± 0.004	0.43 ± 0.006	0.33 ± 0.05	10 ± 1		8±1	7±1	<5
Ho II/sf-1	08:18:48.5 + 70:44:40.1	28×28	880 ± 0.5	1.34 ± 0.008	1.09 ± 0.012	16.69 ± 1.67	319 ± 6	165 ± 5	144±14	79±4	51±4
Ho II/sf-2	08:19:13.3 + 70:42:56.3	28×28	2610 ± 0.5	20.41 ± 0.008	14.19 ± 0.012	46.32 ± 4.63	471 ± 7	497 ± 5	407±39	205±4	103±4
Ho II/sf-3	08:18:57.2 + 70:42:48.4	46×46	4740 ± 0.8	12.31 ± 0.014	8.40 ± 0.020	17.91 ± 1.80	449 ± 7	751 ± 8	630±19	345±7	196±6
Ho II/sf-4	08:19:26.9 + 70:42:27.0	43×43	4780 ± 0.7	10.44 ± 0.013	7.99 ± 0.018	63.18 ± 6.32	765 ± 7	892 ± 7	387±16	247±6	105±5

Notes. [a]Star-forming regions we defined in our EMP galaxies; [b]RA. and Dec. of the centre of each region; [c]Major axis and minor axis of each region in arcseconds; [d]Flux density at far-UV of each region, the same with $f_{3.6\,\mu m}$, $f_{4.5\,\mu m}$, $f_{70\,\mu m}$, $f_{160\,\mu m}$, $f_{250\,\mu m}$, $f_{350\,\mu m}$.

Table 4. Pixel sizes of *Herschel* data used in this paper.

Instrument	Wavelength	Pixel size	Resolution
Herschel/PACS	70, 160 μm	1 arcsec, 2 arcsec	5 arcsec, 13 arcsec
Herschel/SPIRE	250, 350, 500 μm	4 arcsec, 6 arcsec, 8 arcsec	18 arcsec, 25 arcsec, 36 arcsec
Spitzer/IRAC	3.6, 4.5 μm	0.75 arcsec[a], 0.75 arcsec	2.5 arcsec, 2.5 arcsec
Spitzer/MIPS	24 μm	1.5 arcsec	6 arcsec
GALEX/FUV	1516 Å	1.5 arcsec	4.5 arcsec

Notes. [a]The pixel size of the 3.6 μm image of ESO146−G14 is 0.6 arcsec.

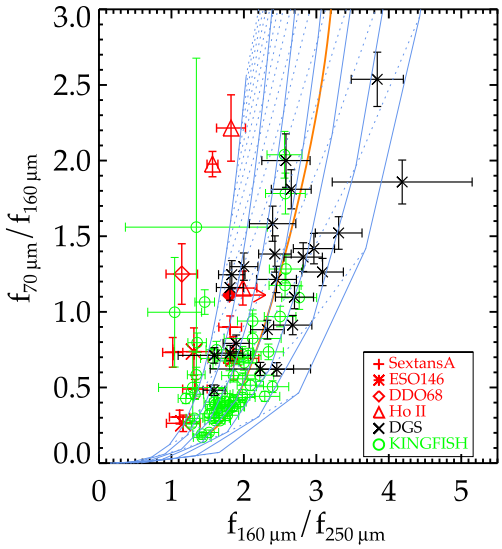

Figure 2. The distribution of EMP star-forming regions, and integrated measurements of galaxies from DGS and KINGFISH in the $f_{70\,\mu m}/f_{160\,\mu m}$ versus $f_{160\,\mu m}/f_{250\,\mu m}$ colour–colour diagram. The grid is a single modified blackbody with a range of temperatures and emissivity indices. The solid line represents a constant emissivity index, β, with the temperature ranging from 10 to 100 K in a decrement of 5 K from the left-bottom to the upper-right. Dashed lines represent constant temperature with β ranging from 0.0 to 3.0 in a step of 0.5 from the left-bottom to the upper-right. The brown line is the trend of star-forming galaxies predicted by the model of Dale et al. (2014).

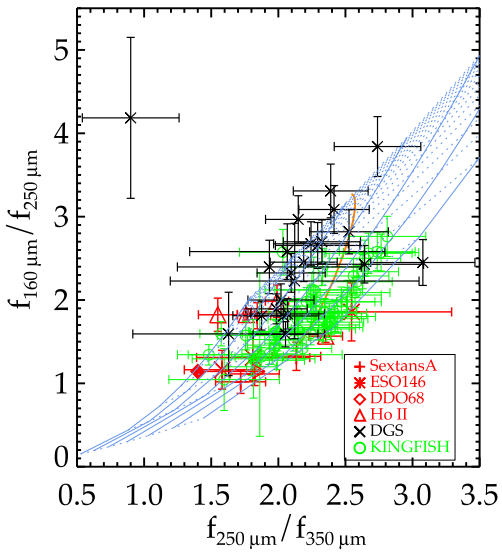

Figure 3. The same as Fig. 2 but using $f_{160\,\mu m}/f_{250\,\mu m}$ versus $f_{250\,\mu m}/f_{350\,\mu m}$.

Table 5. Results of Single MBB Fits to the SEDs at ≥100 μm.

Region	T (K)	β	M_{dust} ($M_\odot$)
SextansA/sf-1	19 ± 8	0.99 ± 1.22	1.34×10^3
SextansA/sf-2	25 ± 9	1.02 ± 0.78	1.31×10^3
SextansA/sf-3	37 ± 17	0.59 ± 0.56	9.93×10^2
SextansA/sf-4	21 ± 9	1.00 ± 1.12	1.21×10^3
ESO146−G14/sf-1	23 ± 22	0.90 ± 2.24	1.00×10^5
ESO146−G14/sf-2	30 ± 5	1.14 ± 0.64	4.51×10^4
ESO146−G14/sf-3	22 ± 16	0.80 ± 1.94	2.11×10^5
Ho II/sf-1	47 ± 13	0.07 ± 0.44	1.98×10^3
Ho II/sf-2	37 ± 4	0.70 ± 0.24	6.03×10^3
Ho II/sf-3	33 ± 1	0.82 ± 0.06	1.30×10^4
Ho II/sf-4	41 ± 1	0.95 ± 0.06	5.42×10^3

bottom-left corner with smaller $f_{160\,\mu m}/f_{250\,\mu m}$ and $f_{250\,\mu m}/f_{350\,\mu m}$. In the figure, there is one object (UM 461) that deviates significantly from the trend. It is difficult to explain such a strange SED. We double checked the photometric measurements and obtained consistent values with those in the literature of Rémy-Ruyer et al. (2013) as used in the figure. But we did notice that the centroids of the 250 and 350 μm images are significantly offset (14 arcsec) from those of the 70 and 160 μm, indicating possible significant contamination by a background source at these two wavelengths.

3.2 MBB fitting

To further characterize the SED shape and understand the dust emission of EMP star-forming regions, the MBB fittings are carried out. A single MBB model fitting to the full SED is not appropriate as a single photon heating dust component may contaminate significantly the 70 μm or even the 100 μm emission. We first performed a single MBB fitting to the photometry ≥100 μm by assuming at these longer wavelengths the contribution from the hot dust component was negligible. The MBB model determined the dust temperature T and the dust emissivity index β from $S_\nu = A{*}B_\nu(T)\lambda^{-\beta}$, where S_ν was the flux density at frequency ν, A was a constant that is related to the column density of the dust, and $B_\nu(T)$ was the Planck function. This method assumed an optically thin condition at the observed far-IR wavelengths with the dust mass derived from $M_{dust} = \frac{S_\nu D^2}{\kappa_\nu B_\nu(T)}$, where κ_ν was the dust opacity, and D was the distance to the galaxy. We took $\kappa_\nu = 1.9$ cm^2 g^{-1} at $\lambda = 350$ μm,[3] and calculated the dust mass at $\lambda = 350$ μm as this band was less sensitive to temperature than shorter wavelengths, and had lower uncertainties than those at longer wavelengths. As listed in Table 5, the single MBB fitting gave a $\beta \sim 1$ and $T \sim$ 20–50 K. The temperature may be underes-

[3] http://www.astro.princeton.edu/~draine/dust/dustmix.html, (Milky Way, R_V = 3.1), Li & Draine (2001).

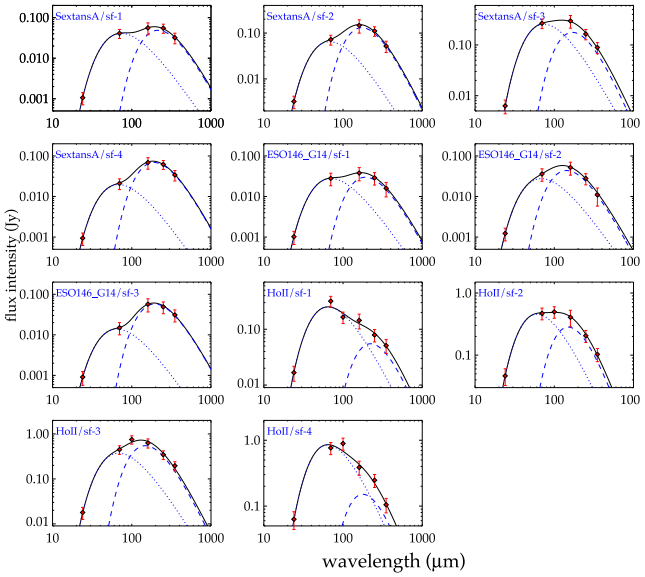

Figure 4. The two modified blackbody fitting to the SEDs. Reds dots are the flux density at different wavelength within each star-forming region. Black solid lines are the 2T MMB best fits with blue dotted lines the best fits of the warm dust components and blue dashed lines the best fits of the cold dust components.

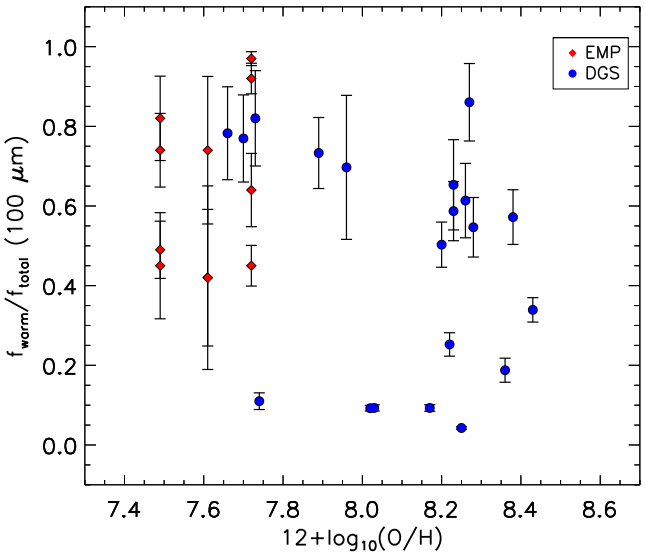

Figure 5. The fraction of warm dust emission at 100 μm as a function of the Oxygen abundance based on the two modified blackbody fitting. The red diamonds are the EMP star-forming regions, and blue circles are for the integrated dwarf galaxies from the DGS.

timated for Sextans A and ESO 146−G14 as there is no 100 μm photometry.

The two-MBB fitting is more reasonable by taking the advantage of the full SED, which is carried out with the equation $S_\nu = A_w * B_\nu(T_w)\lambda^{-\beta_w} + A_c * B_\nu(T_c)\lambda^{-\beta_c}$, where A_w, T_w and β_w describe the hot component of the dust emission while A_c, T_c and β_c are for the cold component. Here, we fixed $\beta_w = 1$ to represent the hot small grains and $\beta_c = 2$ for the cold large grains, similar to the study of Zhu et al. (2009). The results are shown in Fig. 4 and listed in Table 6. The dust mass is derived in the same way as the single MBB fitting. If the cold component dust indices β_c decrease from 2.0 to 1.7, 1.5 and 1.3, the derived T_c increases and the derived dust mass drops by 10 per cent, 25 per cent and 50 per cent, respectively.

Our two MBB fits give cold dust with $T_c \sim 15$–20 K and warm dust with $T_w \sim 50$–60 K. Fig. 4 indicates that the warm dust emission is significant for these EMP star-forming regions, in contrast to those of Spirals (Galametz et al. 2012). To furthermore characterize the importance of the hot dust emission, we performed similar fittings to the integrated SEDs of the DGS sample (Rémy-Ruyer et al. 2013) and investigated the fraction of the emission from the warm dust MBB at 100 μm ($f_{\rm warm}/f_{\rm total})_{100\,\mu\rm m}$ as a function of the oxygen abundance. The result is shown in Fig. 5. It indicates that the fraction $(f_{\rm warm}/f_{\rm total})_{100\,\mu\rm m}$ increases on average with decreasing metallicities: around the Solar abundance, the warm dust emission is small (<20 per cent) but reaches above 50 per cent below 1/10 of the Solar metallicity. Such a high warm dust contribution cautions the single MBB fitting to the photometry for EMP galaxies when the data at $\lambda \leq 100$ μm are included. As shown in Fig. 4, our two-MBB fittings with $\beta = 2$ for the cold component also provide good fittings, while the single MBB requires a lower β. This suggests that the result about β is sensitive to the way how the MBB fitting is performed, and the β of metal-poor galaxies can be underestimated as a result of a large warm dust contribution up to 100 μm.

3.3 Spatial variations of SEDs and dust heating mechanism

Spatially resolved IR data allow us to investigate the spatial variation of the IR SEDs among different star-forming regions in our EMP galaxy sample. As shown in Fig. 2, the variation in the colour $f_{70\,\mu\rm m}/f_{160\,\mu\rm m}$ among different EMP regions for a given galaxy seems to be smaller as compared to the overall scatter of the integrated colour. The $f_{70\,\mu\rm m}/f_{160\,\mu\rm m}$ spans an overall range from

Table 6. Results of two MBB fits to the photometry.

Region	$T_{\rm cold}$ [(K)	$T_{\rm warm}$ (K)	$M_{\rm warm}$ ($M_\odot$)	$M_{\rm cold}$ ($M_\odot$)	$M_{\rm warm}/M_{\rm cold}$	$f_{\rm warm}/f_{\rm total}$(100 μm)	$L_{8-1000\,\mu\rm m}$ ($L_\odot$)
SextansA/sf-1	13 ± 2	49 ± 2	2.22×10^1	3.33×10^3	6.7×10^{-3}	0.82	1.93×10^5
SextansA/sf-2	16 ± 2	54 ± 3	2.49×10^1	3.00×10^3	8.3×10^{-3}	0.49	4.09×10^5
SextansA/sf-3	17 ± 3	49 ± 2	1.43×10^2	3.72×10^3	3.8×10^{-2}	0.74	1.11×10^6
SextansA/sf-4	15 ± 1	53 ± 3	7.74×10^0	2.62×10^3	3.0×10^{-3}	0.45	1.53×10^5
ESO146−G14/sf-1	15 ± 2	52 ± 2	2.78×10^3	2.60×10^5	1.0×10^{-2}	0.74	2.98×10^7
ESO146−G14/sf-2	20 ± 4	53 ± 5	2.50×10^3	8.64×10^4	2.9×10^{-2}	0.42	3.77×10^7
ESO146−G14/sf-3	14 ± 2	56 ± 3	1.00×10^3	5.35×10^5	1.9×10^{-3}	0.42	2.66×10^7
Ho II/sf-1	13 ± 3	56 ± 2	4.19×10^2	2.39×10^4	1.8×10^{-2}	0.97	5.46×10^6
Ho II/sf-2	19 ± 3	60 ± 4	5.81×10^2	1.69×10^4	3.4×10^{-3}	0.64	1.21×10^7
Ho II/sf-3	19 ± 2	53 ± 3	7.68×10^2	3.04×10^4	2.5×10^{-2}	0.45	1.17×10^7
Ho II/sf-4	16 ± 4	57 ± 2	1.36×10^3	2.11×10^4	6.4×10^{-2}	0.92	1.88×10^7

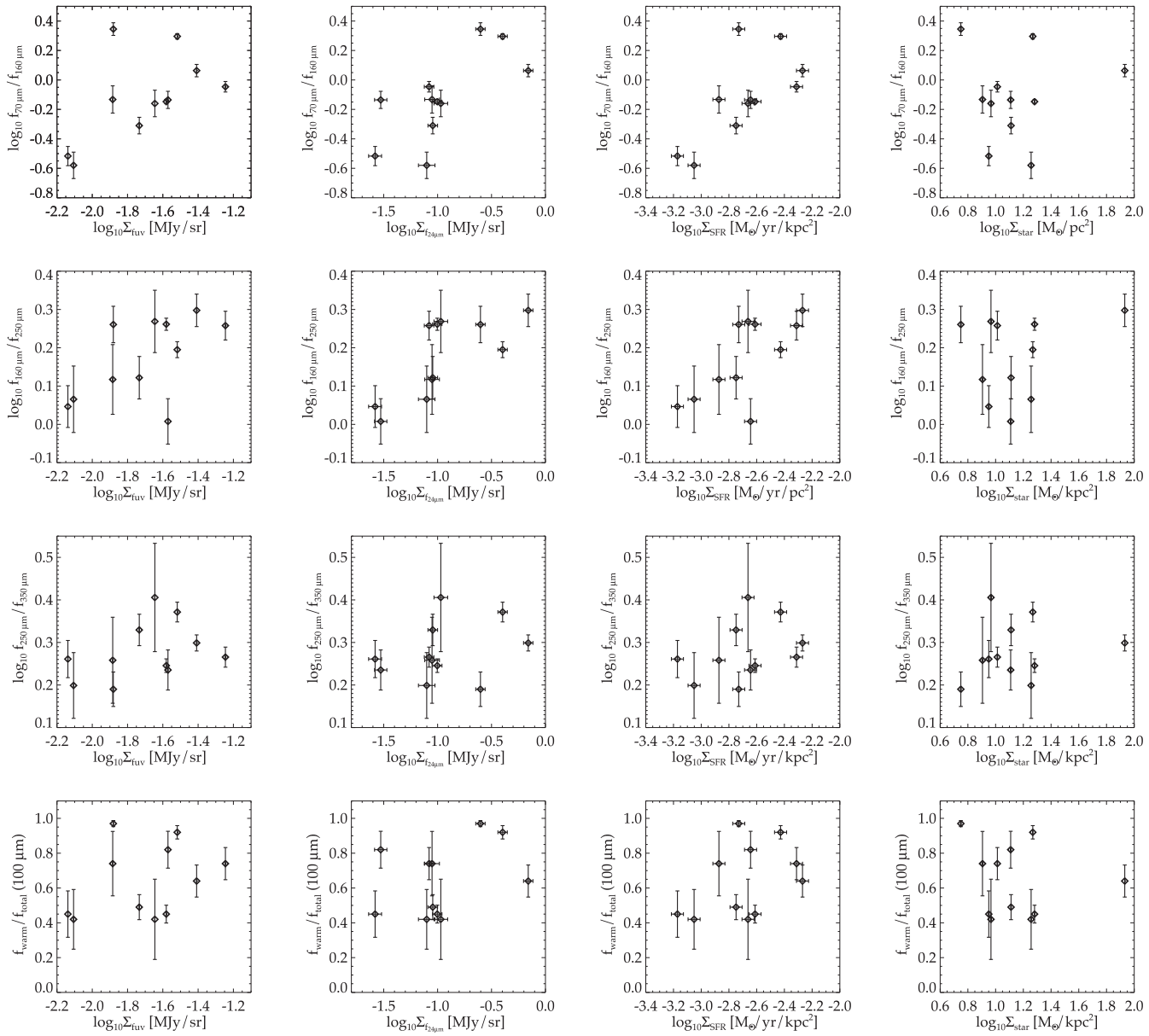

Figure 6. The IR colours as functions FUV surface brightness, 24 μm surface brightness, SFR surface densities and stellar mass surface densities from left to right.

about 0.2–2.5. In contrast, four EMP regions in Sextans A have $f_{70\,\mu m}/f_{160\,\mu m}$ between 0.5 and 1.0, four regions of Ho II span the colour range from 0.7 to 2.3, and three regions of ESO 146−G14 show the colour from 0.2 to 0.7. As shown in Fig. 3, the variation in the colour $f_{160\,\mu m}/f_{250\,\mu m}$ among different EMP regions within a given galaxy is also smaller than the overall scatter among integrated quantities of galaxies.

With the spatially resolved images, we can further study the colour as a function of local conditions in the 2D. In Fig. 6, the far-IR colour of individual EMP regions is investigated as a functions of FUV surface brightness, 24 μm surface brightness, star formation rates (SFRs) and stellar masses.[4] All surface brightness/densities as listed in Table 7 are inclination corrected with angles of 0°, 50°, 54° and 30° for Sextans A, ESO 146−G14, DDO 68 and Ho II, respectively. As indicated by the figure, the FUV surface brightness of our EMP regions are between about 0.01 and 0.1 MJy sr^{-1}, which is within the range of Spirals (Gil de Paz et al. 2007; Shi et al. 2011). The SFR surface densities of our EMP regions are between $10^{-3.5}$ and 10^{-2} $M_\odot$ yr kpc^2. This is also within the range of star-forming regions of local Spirals (Bigiel et al. 2008). The stellar mass surface densities of EMP regions are between 5 and 15 $M_\odot$ kpc^2,

[4] SFRs and stellar masses are estimated following Leroy et al. (2008)'s formula. SFR from Leroy et al. (2008) is calibrated from Spiral galaxies and combines both UV (unobsured) and IR (obscured) maps, which is applicable to low-metallicity galaxies (Calzetti et al. 2007; Salim et al. 2007). For one galaxy (Sextans A), we collected the broad-band photometry (FUV, NUV, V band, 3.6 and 4.5 μm) and derived stellar masses based on the SED fitting. The result is not that different from the one based on Leroy et al. (2008)'s method, with the difference <20 per cent.

Table 7. Measurements of 2D densities of EMP star-forming regions.

Region	$\Sigma_{\rm FUV}$ (MJy sr^{-1})	$\Sigma_{24\,\mu\rm m}$ (MJy sr^{-1})	$\Sigma_{\rm SFR}$ (M$_\odot$ yr^{-1} kpc^{-2})	$\Sigma_{\rm star}$ (M$_\odot$ pc^{-2})	$\Sigma_{\rm dust}$ (M$_\odot$ kpc^{-2})
SextansA/sf-1	$(2.69 \pm 0.018) \times 10^{-2}$	$(2.97 \pm 0.39) \times 10^{-2}$	$(2.27 \pm 0.23) \times 10^{-3}$	$(1.28 \pm 0.007) \times 10^{1}$	$(4.72 \pm 0.47) \times 10^{4}$
SextansA/sf-2	$(1.85 \pm 0.026) \times 10^{-2}$	$(9.01 \pm 0.92) \times 10^{-2}$	$(1.78 \pm 0.18) \times 10^{-2}$	$(1.29 \pm 0.007) \times 10^{1}$	$(3.75 \pm 0.38) \times 10^{4}$
SextansA/sf-3	$(5.69 \pm 0.061) \times 10^{-2}$	$(8.33 \pm 0.85) \times 10^{-2}$	$(4.87 \pm 0.49) \times 10^{-3}$	$(1.03 \pm 0.005) \times 10^{1}$	$(3.85 \pm 0.39) \times 10^{4}$
SextansA/sf-4	$(7.27 \pm 0.668) \times 10^{-3}$	$(2.63 \pm 0.36) \times 10^{-2}$	$(6.73 \pm 0.67) \times 10^{-4}$	$(8.93 \pm 0.070) \times 10^{0}$	$(3.79 \pm 0.38) \times 10^{4}$
ESO146−G14/sf-1	$(1.31 \pm 0.058) \times 10^{-2}$	$(8.88 \pm 0.22) \times 10^{-2}$	$(1.34 \pm 0.13) \times 10^{-3}$	$(8.04 \pm 0.073) \times 10^{0}$	$(9.84 \pm 0.98) \times 10^{4}$
ESO146−G14/sf-2	$(2.26 \pm 0.033) \times 10^{-2}$	$(1.07 \pm 0.24) \times 10^{-1}$	$(2.18 \pm 0.22) \times 10^{-3}$	$(9.26 \pm 0.073) \times 10^{0}$	$(3.59 \pm 0.36) \times 10^{4}$
ESO146−G14/sf-3	$(7.83 \pm 0.096) \times 10^{-3}$	$(7.92 \pm 0.22) \times 10^{-2}$	$(8.88 \pm 0.89) \times 10^{-4}$	$(1.80 \pm 0.007) \times 10^{1}$	$(1.80 \pm 0.18) \times 10^{5}$
Ho II/sf-1	$(1.32 \pm 0.025) \times 10^{-2}$	$(2.50 \pm 0.29) \times 10^{-1}$	$(1.87 \pm 0.29) \times 10^{-3}$	$(5.61 \pm 0.034) \times 10^{0}$	$(6.50 \pm 0.65) \times 10^{5}$
Ho II/sf-2	$(3.90 \pm 0.008) \times 10^{-2}$	$(6.93 \pm 0.80) \times 10^{-1}$	$(5.38 \pm 0.54) \times 10^{-3}$	$(8.55 \pm 0.003) \times 10^{1}$	$(4.01 \pm 0.40) \times 10^{4}$
Ho II/sf-3	$(2.63 \pm 0.007) \times 10^{-2}$	$(9.93 \pm 0.12) \times 10^{-2}$	$(2.45 \pm 0.25) \times 10^{-3}$	$(1.91 \pm 0.002) \times 10^{1}$	$(3.38 \pm 0.34) \times 10^{4}$
Ho II/sf-4	$(3.03 \pm 0.006) \times 10^{-2}$	$(4.01 \pm 0.46) \times 10^{-1}$	$(3.74 \pm 0.37) \times 10^{-3}$	$(1.85 \pm 0.002) \times 10^{1}$	$(2.76 \pm 0.28) \times 10^{4}$

which is several times lower than those of Spirals (e.g. Shi et al. 2011).

Fig. 6 shows that all three IR colours including $f_{70\,\mu\rm m}/f_{160\,\mu\rm m}$, $f_{160\,\mu\rm m}/f_{250\,\mu\rm m}$ and $f_{250\,\mu\rm m}/f_{350\,\mu\rm m}$ increase on average with the increasing FUV surface brightness, 24 μm surface brightness and SFR surface densities, with the best relationships with the SFR surface densities. While all these three surface brightness/densities are associated with young stars, the SFR derived here includes both the unobscured component as traced by the FUV and the obscured one as traced by the 24 μm. Fig. 6 furthermore shows that there are no trends between the IR colours and the stellar mass surface densities. Unlike the SFR, the stellar mass is better related to old stars. Investigations of the relationships between the far-IR colours and the tracers can be used to constrain if the dust is mainly heated by the radiation from the young stars or the interstellar radiation field from the old stars. As argued by Bendo et al. (2015), such investigations show many advantages in understanding the dust heating mechanism as compared to other methods such as the dust SED fitting and radiative transfer that relies on assumptions of dust grain properties, SED shapes of heating source etc. The results of Fig. 6 thus support that young stars are the main heating source of dust radiating at wavelengths from 70 μm to ≥250 μm in EMP star-forming regions. Investigations of the heating source of dust in Spirals by Bendo et al. (2015) found that in only 3 out of 24 galaxies, the $f_{160\,\mu\rm m}/f_{250\,\mu\rm m}$ and $f_{250\,\mu\rm m}/f_{350\,\mu\rm m}$ are better related to the SFRs than old stars while in the remaining the $f_{250\,\mu\rm m}/f_{350\,\mu\rm m}$ colour is driven by both.

The above result suggests that the dust of emission at 70 μm up to 350 μm in EMP regions is heated by young stars instead of diffuse stellar radiation from old stars. The underlying cause for this needs further investigations. As discussed above, the SFR surface densities of our EMP regions are not that different from those in Spirals, indicating the radiation fields from young stars are not enhanced in EMP regions compared to star-forming regions in Spirals. But the SFR relative to the stellar mass, i.e. the specific SFR (sSFR), in these EMP regions is enhanced, with the median of log(sSFR[Gyr^{-1}]) around −0.82 and a standard deviation of 0.36. In contrast, the star-forming regions of 12 Spirals in Shi et al. (2011) have the median log(sSFR[Gyr^{-1}]) of −1.28 and a standard deviation of 0.32. Compared to the sSFRs of dwarf galaxies as studied by Hunt et al. (2015), our galaxies lie below their trend, but still within the scatter (0.01–30 Gyr^{-1}, around metallicities of our galaxies). This difference could be due to the fact that our galaxies are mostly dwarf irregulars and low-surface brightness galaxies, while the sample of Hunt et al. (2015) contains many blue compact dwarf galaxies that are known to be compact with enhanced SFRs and have higher sSFRs due to interactions.

The properties of dust grains in EMP galaxies may be systematically different from those in Spirals, making the heating from young stars important to the dust emission all the way up to 350 μm. For example, if small dust grains in EMP galaxies are abundant, they could be heated to higher temperatures without requiring an enhanced radiation field. It is observationally difficult to quantify the size of dust grains. Studies of extinction curves point out that metal-poor dwarfs in the Local Group, Small Magellanic Cloud and Large Magellanic Cloud, show more steeply rising extinction at UV wavelengths, suggesting smaller dust grains in these two galaxies (for a review, see Li et al. 2015). A simple extrapolation of this result into the EMP regime would naturally expect the dust in EMP galaxies to be smaller due to the lack of raw material for grain growth. Small grains could offer more surface area for the formation of molecular hydrogen that is likely abundant in EMP galaxies as indicated by several tracers including dust (e.g. Shi et al. 2014), warm H_2 (e.g. Hunt et al. 2010) and [C II] 158 μm (e.g. Madden et al. 1997, 2013) although CO is very weak (e.g. Shi et al. 2015). However, it is impossible with current facilities to obtain the measurements of the extinction curve for these relatively distant EMP galaxies, and thus to conclude the size of dust grains in EMP galaxies.

4 DUST-TO-STELLAR MASS RATIO

In Fig. 7, the dust-to-stellar mass ratio of our EMP regions are plotted against the oxygen abundance, 12+log(O/H), along with the integrated quantities from the DGS. The dust masses of both samples are measured using the same method, i.e. the two MBB fitting (see Section 3.2), which could avoid the artificial effects of different dust mass estimates on the relationship. As shown in the figure, there does not seem to exist any correlation between these two quantities. Hunt et al. (2014) also found that two EMP galaxies (IZw 18 and SBS 0335-052) show very different dust-to-stellar mass ratio although both are similarly very metal-poor, and their ratios lie within the overall scatter of spiral and other dwarfs at higher metallicities. Our significantly increased number of the data points in the EMP regime as compared to the work of Hunt et al. (2014) allows us to derive conclusive results that the dust-to-stellar mass ratio is not related to the metallicity. The figure furthermore indicates that even within a given galaxy, the dust-to-stellar mass ratio of individual EMP regions could show large scatters, e.g. EMP regions in Ho II span the whole range from roughly 10^{-4}–10^{-2}, while EMP regions in Sextans A and ESO 146−G14 have much smaller scatters.

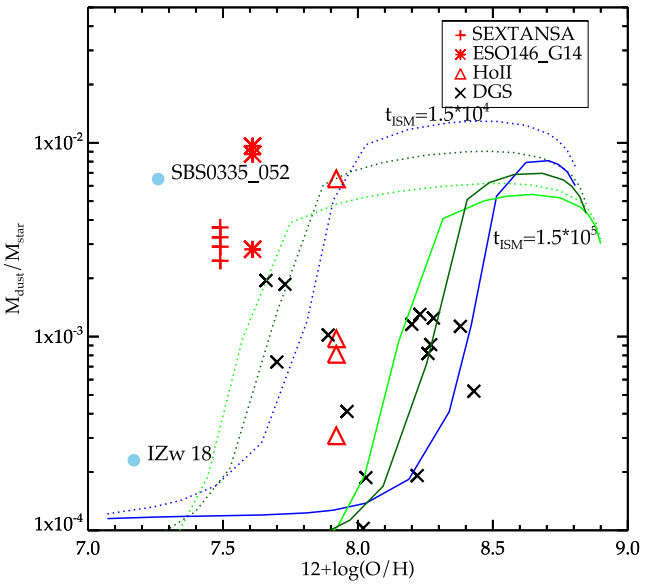

Figure 7. The dust-to-stellar mass ratio of our EMP star-forming regions and integrated galaxies of the DGS. The lines are the model predictions by Feldmann (2015). t_{ISM} is the dust growth time-scale which can be computed from basic collision theory (Weingartner & Draine 1999) (solid or dashed lines). Q_{MS} denotes the (multiplicative) offset of a given galaxy from the main sequence (blue: 1/3, cyan: 1, green: 3). The data for IZw 18 and SBS 0335-052 are from Hunt et al. (2014).

The overlaid lines in Fig. 7 are the predictions of the model by Feldmann (2015, private communication), where t_{ISM} is the dust growth time-scale which can be derived from Weingartner & Draine (1999)'s basic collision theory (solid or dashed lines). Blue, cyan and green lines refer to Q_{MS} = 1/3, 1, 3, which denote the (multiplicative) offset of a given galaxy from the main sequence. While the normalization of the trend depends on the methodology used for dust mass and metallicity measurements, the model-predicted sharp drop between 1/10 and 1/5 solar abundance is clearly not seen in Fig. 7. The model of Feldmann (2015) invokes gas outflow, inflow and star formation in an equilibrium state in order to reproduce the observed dust-to-gas mass ratio as a function of metallicity as well as many other observed galaxy properties. The model is motivated to explain the observed sharp drop in the dust-to-gas mass ratio versus the metallicity around 20 per cent solar metallicity (Rémy-Ruyer et al. 2014; Shi et al. 2014). Fig. 7 indicates that although a sharp drop may occur in the dust-to-gas ratio, a similar drop in the trend of the dust-to-stellar ratio as a function of metallicity is not seen. The model argues that the dust content in EMP galaxies is mainly regulated by the galactic outflow, whose efficiency may be overestimated so that too much dust is removed relative to the stellar content. Our results furthermore suggest that if outflows regulate the dust-to-stellar mass ratio, they must vary greatly on scales of 100–1000 pc.

5 CONCLUSIONS

We present IR SEDs of individual star-forming regions in four EMP galaxies observed by *Herschel*. The main conclusions are as follows.

(1) As compared to spirals and higher metallicity dwarfs, EMP star-forming regions have on average much higher $f_{70\,\mu m}/f_{160\,\mu m}$ ratios at given $f_{160\,\mu m}/f_{250\,\mu m}$ ratios. In addition, single MBB fits to the SED at $\lambda \geq 100$ μm show higher dust temperatures and lower emissivity indices, while two-MBB fits with a fixed emissivity index show that even at 100 μm about half of the emission comes from warm (∼50 K) dust, unlike that seen in Solar metallicity spiral galaxies.

(2) Our spatially resolved images furthermore reveal that the far-IR colours including $f_{70\,\mu m}/f_{160\,\mu m}$, $f_{160\,\mu m}/f_{250\,\mu m}$ and $f_{250\,\mu m}/f_{350\,\mu m}$ are all related to the surface densities of young stars (FUV, 24 μm and SFRs), but not with the stellar mass surface densities. This suggests that the dust emitting at wavelengths from 70 μm all the way up to the 350 μm is heated by radiation from young stars instead of old stars.

(3) Our EMP regions cover a large range in the dust-to-stellar mass ratio, indicating the importance of local conditions, such as outflows etc., in regulating the dust content.

ACKNOWLEDGEMENTS

We thank the anonymous referee for helpful suggestions that improved the quality of the paper. LZ and YS acknowledge support for this work from the National Natural Science Foundation of China (grant 11373021), the Strategic Priority Research Program 'The Emergence of Cosmological Structures' of the Chinese Academy of Sciences (grant No. XDB09000000), and Excellent Youth Foundation of Jiangsu Scientific Committee (grant BK20150014). LZ also thanks for the support by the National Natural Science Foundation of China (Grant No. J1210039). AL is supported in part by NSF AST-1311804 and NASA NNX14AF68G. This research has made extensive use of the NASA/IPAC Extragalactic Database (NED) which is operated by the Jet Propulsion Laboratory, California Institute of Technology, under contract with the National Aeronautics and Space Administration. This work is based (in part) on observations made with the *Spitzer Space Telescope*, which is operated by the Jet Propulsion Laboratory, California Institute of Technology under a contract with NASA.' The *Galaxy Evolution Explorer* (*GALEX*) is a NASA Small Explorer, launched in 2003 April. We acknowledge NASA's support for construction, operation, and science analysis for the *GALEX* mission.

REFERENCES

Allende Prieto C., Lambert D. L., Asplund M., 2001, ApJ, 556, L63
Aloisi A. et al., 2007, ApJ, 667, L151
Bendo G. J. et al., 2015, MNRAS, 448, 135
Bergvall N., Ronnback J., 1995, MNRAS, 273, 603
Bigiel F., Leroy A., Walter F., Brinks E., de Blok W. J. G., Madore B., Thornley M. D., 2008, AJ, 136, 2846
Calzetti D. et al., 2007, ApJ, 666, 870
Casasola V., Hunt L., Combes F., García-Burillo S., 2015, A&A, 577, A135
Croxall K. V., van Zee L., Lee H., Skillman E. D., Lee J. C., Côôté S., Kennicutt R. C., Jr, Miller B. W., 2009, ApJ, 705, 723
Dale D. A., Helou G., Magdis G. E., Armus L., Dííaz-Santos T., Shi Y., 2014, ApJ, 784, 83
Draine B. T., Li A., 2001, ApJ, 551, 807
Draine B. T., Li A., 2007, ApJ, 657, 810
Engelbracht C. W., Gordon K. D., Rieke G. H., Werner M. W., Dale D. A., Latter W. B., 2005, ApJ, 628, L29
Engelbracht C. W., Rieke G. H., Gordon K. D., Smith J.-D. T., Werner M. W., Moustakas J., Willmer C. N. A., Vanzi L., 2008, ApJ, 678, 804
Feldmann R., 2015, MNRAS, 449, 3274
Fisher D. B. et al., 2014, Nature, 505, 186
Galametz M. et al., 2012, MNRAS, 425, 763
Gil de Paz A. et al., 2007, ApJS, 173, 185
Griffin M. J. et al., 2010, A&A, 518, LL3
Hunt L. K., Thuan T. X., Izotov Y. I., Sauvage M., 2010, ApJ, 712, 164

Hunt L. K. et al., 2014, A&A, 561, A49
Hunt L. K. et al., 2015, A&A, 583, A114
Izotov Y. I., Thuan T. X., 1999, ApJ, 511, 639
Izotov Y. I., Thuan T. X., Lipovetsky V. A., 1997, ApJS, 108, 1
Kennicutt R. C. et al., 2011, PASP, 123, 1347
Kniazev A. Y., Grebel E. K., Pustilnik S. A., Pramskij A. G., Zucker D. B., 2005, AJ, 130, 1558
Kunth D., Oumlstlin G., 2000, A&AR, 10, 1
Leroy A. K., Walter F., Brinks E., Bigiel F., de Blok W. J. G., Madore B., Thornley M. D., 2008, AJ, 136, 2782
Li A., Draine B. T., 2001, ApJ, 554, 778
Li A., Wang S., Gao J., Jiang B. W., 2015, preprint (arXiv:1507.06604)
McCall M. L., Vaduvescu O., Pozo Nunez F., Barr Dominguez A., Fingerhut R., Unda-Sanzana E., Li B., Albrecht M., 2012, A&A, 540, A49
Madden S. C., Poglitsch A., Geis N., Stacey G. J., Townes C. H., 1997, ApJ, 483, 200
Madden S. C. et al., 2013, PASP, 125, 600
Poglitsch A. et al., 2010, A&A, 518, LL2
Pustilnik S. A., Kniazev A. Y., Pramskij A. G., 2005, A&A, 443, 91
Rémy-Ruyer A. et al., 2013, A&A, 557, A95
Rémy-Ruyer A. et al., 2014, A&A, 563, A31
Rosenberg J. L., Wu Y., Le Floc'h E., Charmandaris V., Ashby M. L. N., Houck J. R., Salzer J. J., Willner S. P., 2008, ApJ, 674, 814
Salim S. et al., 2007, ApJS, 173, 267
Shi Y., Helou G., Yan L., Armus L., Wu Y., Papovich C., Stierwalt S., 2011, ApJ, 733, 87
Shi Y., Armus L., Helou G., Stierwalt S., Gao Y., Wang J., Zhang Z.-Y., Gu Q., 2014, Nature, 514, 335
Shi Y., Wang J., Zhang Z.-Y., Gao Y., Armus L., Helou G., Gu Q., Stierwalt S., 2015, ApJ, 804, L11
Weingartner J. C., Draine B. T., 1999, ApJ, 517, 292
Wu Y., Charmandaris V., Hao L., Brandl B. R., Bernard-Salas J., Spoon H. W. W., Houck J. R., 2006, ApJ, 639, 157
Zhu M., Papadopoulos P. P., Xilouris E. M., Kuno N., Lisenfeld U., 2009, ApJ, 706, 941

This paper has been typeset from a TEX/LATEX file prepared by the author.